Facile fabrication of dye-sensitized solar cells utilizing carbon nanotubes grown over 2D hexagonal bimetallic ordered mesoporous materials

J. Balamurugan [a], R. Thangamuthu [b], A. Pandurangan [a,*], M. Jayachandran [b]

[a] Department of Chemistry, Institute of Catalysis and Petroleum Technology, Anna University, Chennai 600 025, TN, India
[b] Electrochemical Materials Science Division, CSIR-Central Electrochemical Research Institute, Karaikudi 630 006, India

HIGHLIGHTS

▶ Well-graphitized CNTs with uniform diameter grown over bimetallic Fe–Cr-SBA-15.
▶ Charge-transfer resistance (R_{ct}) of CNTs was lower than that of Pt.
▶ CNTs counter electrode based DSSCs showed higher solar to electric efficiency.
▶ CNTs are suitable alternative cathode material to replace Pt in DSSCs.

GRAPHICAL ABSTRACT
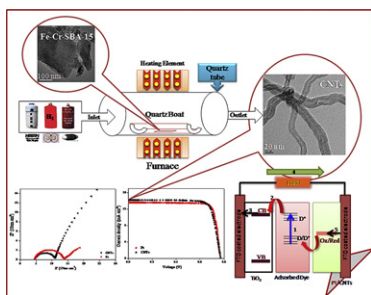
ARTICLE INFO

ABSTRACT

High-surface area and well-ordered mesoporous Fe incorporated SBA-15 (Fe-SBA-15), Fe–Cr incorporated SBA-15 (Fe–Cr-SBA-15) and Cr incorporated SBA-15 (Cr-SBA-15) catalysts are synthesized following a controlled post synthesis grafting process. The activities of all the catalysts are tested systematically and quantitatively towards the production of carbon nanotubes (CNTs) by chemical vapour deposition. In order to obtain CNTs with high quality and quantity, the parameters like temperature, reaction time and gas flow rate are optimized. Under optimum conditions, the Fe–Cr-SBA-15 catalyst is produced with high yield and uniform diameter of CNTs. The transmission electron microscopy result reveals high purity and well-graphitized structure of CNTs. The synthesized CNTs are used as counter electrode material for dye-sensitized solar cells (DSSCs). The CNTs based counter electrode shows good chemical stability, lower charge-transfer resistance and higher electrocatalytic activity towards I_3^-/I^- redox reaction than that of platinum (Pt) counter electrode. The energy conversion efficiency of the CNTs counter electrode based DSSCs reaches 8.86% under irradiation with a simulated solar light intensity of 100 mW cm^{-2}. The results prove that CNTs are one of the suitable candidates for Pt free counter electrode for DSSCs.

© 2012 Elsevier B.V. All rights reserved.

1. Introduction

Due to the low fabrication cost and relatively high efficiency of dye-sensitized solar cells (DSSCs) they are being considered as an alternative to traditional silicon-based solar cells [1,2]. The counter electrode in DSSCs is one of the essential components, as it plays a crucial role in collecting electrons from the external circuit and reducing I_3^- to I^- in the electrolyte [3,4]. At present, platinum (Pt) thin film is mainly used as the counter electrode in DSSCs due to its high electrical conductivity and good electrochemical catalytic activity for I_3^- reduction [5]. The high cost, poor stability in corrosive electrolytes, and high processing temperatures has led to the

* Corresponding author. Tel.: +91 44 22358653; fax: +91 44 22200660.
E-mail address: pandurangan_a@yahoo.com (A. Pandurangan).

innovation of novel alternatives either in the existing or as a whole in the counter electrode materials [6]. Recently, carbon nanotubes (CNTs), an important member in carbon family, have been found to be an alternative source for counter electrodes in DSSCs instead of Pt due to their satisfying features such as low cost, large surface area, superior chemical stability, and good catalytic activity [7].

At present, several methods have been reported for the fabrication of CNTs counter electrodes, such as drop-coating [8], chemical vapour deposition [9], screen-printing [10] and spray coating [11]. Considering the cost and versatile processing techniques, spin-coating seems to be the most reliable method in the aspect of potential technological applications. This method has been used to deposit the thin layer on the surface of conductive glass substrate. The thin layer obtained by spin-coating from suspension exhibits distinct advantages, such as high dispersion rate, excellent uniformity and controlled thickness. CNTs counter electrodes prepared by this method is necessary because of their appreciable performance in practical applications. The successful synthesis of high purity CNTs with uniform diameter is the critical step towards their applications. Despite enormous work on the synthesis of CNTs, high purity with uniform diameter CNTs that congregate the quality and quantity requirements for their high performance applications are still lacking. This has become the major obstacle currently to some of their high performance applications. CNTs with uniform diameter have now widely attracted the interest in electronic memory device, biosensors, solar cells and drug delivery applications. CNTs synthesized with large amounts of nanotubes with uniform size and structure thus require separation of the desired tubes from a complex mixture and subsequent alignment.

The discovery of mesoporous silica molecular sieves opened up new possibilities in many areas of chemistry and material science [12]. These materials possess high specific surface areas, high pore volume and well-ordered pore structures with uniform mesopores, adjustable from about 2 to 10 nm. Mesoporous materials have a clear advantage over microporous zeolites and zeotype molecular sieves for the growth of CNTs at high temperatures. The M41S mesoporous materials offer an opportunity for them to be used as versatile catalysts or catalyst supports for the conversion of large molecules, but their weak hydrothermal stability greatly limits their extensive use. Many efforts have been made to improve the stability of mobil composition of matter no. 41 (MCM-41). During the last decade, santa barbara amorphous no. 15 (SBA-15) has been extensively studied [12] and is being evaluated for numerous applications in the fields of catalysis, separations, ion exchange and nanotechnology. The desirable features of SBA-15, including tailored pore size, high degree of structural ordering, ease of fabrication, large pore size, thick pore walls and high hydrothermal stability in comparison with MCM-41 creates remarkable interest in research [12,13]. The polymer employed to obtain SBA-15, poly(ethylene oxide)–poly(propylene oxide)–poly(ethylene oxide), is biodegradable and cheaper than the surfactants used initially in the synthesis of MCM-41 is desirable. The additional feature of SBA-15 is the existence of micropores interconnecting hexagonally ordered mesopores, which makes it more suitable for catalysis. The interconnections facilitate diffusion inside the entire porous structure. A simple way to functionalize the silica SBA-15 is to introduce active metal ions in silica matrix either during the synthesis or by post synthesis modification of SBA-15. It is very difficult to incorporate metal ions into SBA-15 directly under the strong acidic conditions because the metal ions exist as cations and the formation of corresponding M–O–Si bonds and effective inclusion in the structure becomes difficult. Several studies have been dedicated to the investigation of transition metal loaded SBA-15 because of their wide range of applications in catalysis.

Specifically Co, Ni, and Fe loaded SBA-15 materials are of interest due to their activity and selectivity for the growth of CNTs.

Hydrocarbons such as methane, ethylene and acetylene have been widely used for the formation of CNTs. Moreover, acetylene is more preferred for the growth of well-graphitized and high quality CNTs rather than any other gaseous hydrocarbons. Compared to Co and Ni used for CNTs synthesis, Fe was reported [14,15] for its highest activity in the decomposition of acetylene. In general, hydrocarbon gases are more common but the use of acetylene is preferred for scale up production of CNTs. Acetylene is considered as a favourable carbon source for CNTs production because of its atom efficiency and higher activity in comparison to other hydrocarbons such as benzene [16]. Duxiao and co-workers [17] demonstrated the use of Fe-impregnated mesoporous molecular sieve as a catalytic template to produce CNTs via this method.

In the present study, high-surface area and well-ordered mesoporous Fe–Cr–SBA-15 catalyst is prepared by post synthesis grafting process through atomic layer deposition method. Similarly, Fe-SBA-15 and Cr-SBA-15 catalysts are also prepared for comparison. These catalysts are characterized by X-ray diffraction pattern (XRD), N_2 sorption isotherm and transmission electron microscopy (TEM) technique and used for CNTs synthesis. Attempts are made to develop the DSSCs using Pt free counter electrode namely well-graphitized CNTs by spin-coating. In parallel, Pt counter electrode also fabricated for comparison. The DSSCs of this CNTs counter electrode exhibits comparable performance with those of Pt. CNTs counter electrode possess lower charge-transfer resistance and higher electrocatalytic activity for the I_3^-/I^- redox reaction compared to Pt counter electrode. The result demonstrates that the CNTs are suitable materials for replacing Pt from counter electrode and will be advantageous for large scale production of DSSCs.

2. Experimental

2.1. Materials

Iron (III) acetylacetonate ($Fe(C_5H_7O_2)_2$), chromium (III) acetylacetonate ($Cr(C_5H_7O_2)_2$) and tetraethylorthosilicate (TEOS) were purchased from Aldrich and used as the precursors for iron, chromium and silicon, respectively. Triblock copolymer poly(ethylene glycol)-block-poly(propylene glycol)-block-poly(ethylene glycol) (Pluronic P123; Mav = 5800, Aldrich) used as a structure-directing agent under acidic conditions. Anhydrous toluene ($C_6H_5CH_3$), ethanol, HCl, acetonitrile (AN) and acetic acid were purchased from Merck. Chloroplatinic acid (H_2PtCl_6), iodine, lithium iodide, 4-tert-butyl-pyridine (TBP), ethyl cellulose, terpineol and N719 dye [cis-di(thiocyanato)-N,N-bis(2,2′-bipyridyl-4-carboxylic acid-4-tetrabutylammonium carboxylate) ruthenium (II)] were purchased from the Aldrich. All the reagents were used without further purification. Fluorine-doped tin oxide (FTO) conducting glass plates (sheet resistance 15 Ω sq^{-1}) were purchased from Xinyan Technology Ltd, HK. The FTO glass substrate was ultrasonicated thoroughly in acetone, ethanol and double distilled water for 15 min in each step to remove organic and other contamination.

2.2. Synthesis of the catalyst

Siliceous SBA-15 mesoporous material was synthesized according to the reported procedure [12]. 4 g of P123 was dissolved in the mixture of 30 mL of double distilled water and 120 mL of 2 N HCl was added under stirring. 8.5 g of TEOS was added dropwise to the solution at 40 °C. The mixture was stirred continuously for 24 h and transferred to Teflon lined stainless steel autoclave and placed in an oven at 100 °C for 48 h. After cooling to room temperature the

resulting solid was recovered by filtration, washed with distilled water and dried under ambient condition for 12 h. The synthesized powder was heated at a constant ramping rate from room temperature to 540 °C over 5 h under nitrogen (N_2) atmosphere and kept for 1 h in the same conditions followed by calcination at 540 °C for 6 h under air to remove the residual organic template materials.

The Fe, Fe–Cr and Cr with 6 wt.% grafted SBA-15 catalysts were synthesized following the controlled grafting process through ALD. Synthesis of 6 wt.% Fe-SBA-15 catalyst was performed as follows. The calcined siliceous SBA-15 sample was suspended in anhydrous toluene and refluxed under N_2 atmosphere for 5 h to remove the adsorbed moisture. Subsequently, an appropriate amount of Iron (III) acetylacetonate dissolved in toluene was added dropwise to the above suspension. The grafting process was performed under N_2 atmosphere by refluxing at 110 °C for 8 h, involving the reaction of Iron (III) acetylacetonate with surface silanol groups of the calcined siliceous SBA-15. The resulting mixture was cooled, filtered and washed with toluene and then dried at room temperature for 12 h. The grafted sample was calcined following the same procedure as mentioned for the preparation of pure siliceous SBA-15 to obtain the final sample denoted as wt.% Fe-SBA-15, where wt.% represents the final Fe content in the sample tested by inductive coupled plasma-atomic emission spectroscopy (ICP-AES) analysis. In a similar way, 6 wt.% Fe–Cr-SBA-15 (1:1) molar ratio and 6 wt.% Cr-SBA-15 catalysts were synthesized.

2.3. Synthesis and purification of CNTs

CNTs growth was carried out in a temperature controlled horizontal tubular furnace at atmospheric pressure. For each growth, 100 mg of the catalyst powder was spread on quartz boat and placed in the centre of a quartz tube. The catalyst was activated by passing argon (Ar) gas. Prior to reaction, the catalyst was reduced under hydrogen at 700 °C for 30 min at atmospheric pressure to generate Fe, Cr and Fe–Cr nanoparticles with the silica supports and then purged with Ar for another 30 min to remove traces of hydrogen. Immediately, the temperature was raised to 700, 800 and 900 °C, respectively in the presence of Ar gas. The CNTs were grown at fixed temperature and flow of argon and varying acetylene flow rate. The flow rates of the gases were controlled using Alicate mass flow controllers. The furnace was cooled to room temperature by maintaining Ar flow after the growth. The following Eq. (1) was used for the determination of percentage of carbon deposited from the catalytic decomposition of acetylene.

$$\text{Carbon deposits yield}(\%) = (m_{\text{tot}} - m_{\text{cat}})/m_{\text{cat}} \times 100 \tag{1}$$

where m_{cat} and m_{tot} are the mass of the catalyst before and after the reaction, respectively.

The synthesized CNTs were purified to remove impurities such as silica matrix, metal particles, amorphous carbon and some carbonaceous materials by an efficient treatment. The catalyst was purified by acid treatment. The synthesized CNTs were placed in 50 mL of 5% HF under sonication for 30 min at ambient temperature; the solid was filtered to remove silica matrix and metal particles. The solid was refluxed at 120 °C in a 4 N nitric acid (HNO_3) solution for 12 h, cooled, filtered and washed with distilled water until the colour of the filtrate became colourless to remove amorphous carbon and residual metal particles. The solid was heated at 400 °C in atmospheric air for 30 min and again treated with 5% HF, to remove the rest of the impurities. The purified CNTs were characterized by TEM, Raman spectroscopy, XRD and thermogravimetric analysis (TGA) techniques.

2.4. Preparation of TiO₂ thin-film photoanode for DSSCs

TiO_2 thin-film photoanode was fabricated by spin-coating technique for DSSCs. The procedure was as follows: 0.5 mL of acetic acid and 3 g TiO_2 (P25, Degussa) powder was mixed in an agate mortar. 2.5 mL double distilled water and 15 mL ethanol were added dropwise into the agate mortar. The mixture was transferred to a beaker containing 25 mL of ethanol and stirred for 1 h followed by ultrasonication about 30 min. Terpineol and ethyl cellulose in ethanol were added to it. Subsequently the above mixture was kept for 24 h in an ultrasonic water bath at 28 °C to obtain well-dispersed TiO_2 paste. The paste was spin coated on cleaned FTO conducting substrate (0.25 cm × 0.25 cm) at 1000 rpm for 20 s and dried at 60 °C for 10 min in oven. TiO_2 was spin coated again at 1000 rpm for 5 s and dried at 60 °C for 10 min. The TiO_2 spin-coated FTO was sintered at 500 °C for 30 min. The TiO_2 thin-film is immersed in 50 mL of 0.5 mM ethanolic N719 dye solution for 24 h in dark at room temperature. The film was cleaned with ethanol and dried in oven to use as a photoanode (working electrode) in DSSCs.

2.5. Preparation of counter electrodes for DSSCs

Pt counter electrode was fabricated on FTO by spin-coating technique. H_2PtCl_6 was dispersed in terpineol solution containing 5 wt.% ethyl cellulose. The paste was spin coated on cleaned FTO conducting substrate at 1000 rpm for 20 s and dried at 60 °C for 10 min in oven. The spin coated thin-film was heated at 385 °C for 20 min. CNTs counter electrode was fabricated on FTO by similar procedure. CNTs were ground in terpineol solution containing of 5 wt.% ethyl cellulose. The paste was spin coated on cleaned FTO conducting substrate at 1000 rpm for 20 s and dried at 60 °C for 10 min in oven. The CNTs coated film was heated at 300 °C for 15 min to maintain good adhesion between the CNTs layer and the FTO substrate. The optimum temperature was 300 °C for the fabrication of CNTs layer on FTO. If the temperature exceeds higher than 350 °C, the terpineol and ethyl cellulose was completely peeled off as reported in Ref.[18]. It was realized that the optimized annealing temperature was 300 °C to increase the adhesion between the CNTs and FTO glass plate.

2.6. Characterization and measurement

The amount of the metal incorporated SBA-15 was analyzed by ICP-AES (Perkin Elmer OPTIMA 3000). The XRD patterns of all the samples were recorded with a PANalytical X'Pert diffractometer, using nickel-filtered CuKα radiation ($\lambda = 1.54$ Å) and a liquid nitrogen-cooled germanium solid-state detector. The diffractograms were recorded in the 2θ range of 0.5–10° for the catalyst and 10–80° for the CNTs. The peaks were identified with reference to compilation of simulated XRD powder patterns. The surface area, pore volume and pore size distribution were measured by N_2 sorption at −197 °C using an ASAP-2010 porosimeter from Micromeritics Corporation. The samples were degassed at 200 °C and 1.3×10^{-3} Pa 8–10 h prior to the adsorption experiments. The mesopore volume was estimated from the amount of N_2 adsorbed at a relative pressure by assuming that all the mesopores were filled with condensed nitrogen in the normal liquid state. Pore size distribution was estimated using the Barret–Joyner–Halenda (BJH) algorithm (ASAP-2010) available as built-in software from Micromeritics. TGA measurements were carried out under atmospheric air using a high-resolution TA Instrument, SDT Q600. The samples for TEM analysis were initially dispersed in ethanol or acetone by ultrasonicating for 30 min which was allowed to settle. A drop of the supernatant liquid was then transferred to carbon coated

copper grid and mounted onto the TEM (JEOL 3010) operated at 300 kV and the micrographs were recorded. The Raman scattering was excited in infrared at 1064 nm with Nd:YAG laser, equipped with liquid nitrogen cooled charge-coupled array detector at 200 mV. Raman spectra were recorded with a Micro-Raman system RM 1000 Renishaw using a laser excitation wavelength at 532 nm (Nd-YAG), 0.5–1 mW, with 1 μm focus spot in order to avoid photodecomposition of the samples.

The electrochemical experiments were carried out using an electrochemical workstation (Autolab PGSTAT 302N). Cyclic voltammograms (CV) were recorded in a three electrode cell Pt/CNTs coated FTO as working electrode, the standard calomel electrode as reference electrode and Pt as counter electrode, respectively. The electrolyte was composed of 10 mM LiI, 1 mM I_2, and 0.1 M $LiClO_4$ in acetonitrile solution [19]. For electrochemical impedance spectroscopy (EIS) measurement, a thin layer symmetric cell was fabricated by clamping two identical CNTs/Pt coated FTO electrodes on each other with Surlyn thermosetting spacer. The electrolyte composition of 0.1 mM LiI, 0.05 M I_2 and 0.5 M 4-tertiary butyl pyridine in acetonitrile was filled between the two electrodes before clamping. The measurement was carried out by AC impedance analyzer from 0.1 Hz to 100 kHz with perturbation amplitude of 10 mV. DSSC was fabricated by clamping a dye-sensitized TiO_2 electrode and CNTs/Pt counter electrode. Surlyn thermosetting spacer was kept between photoanode and counter electrode. Before clamping, the active area (0.25 cm^2) was filled with similar electrolyte used in EIS measurement. The photovoltaic performance parameters of DSSCs were measured under light intensity of 100 mW cm^{-2}.

3. Results and discussion

3.1. Characterization of synthesized catalysts

3.1.1. X-ray diffraction pattern

The percentages of metal present in Fe-SBA-15, Fe–Cr-SBA-15 and Cr-SBA-15 catalysts were estimated from the ICP-AES measurement and the results are shown in Table 1. The low angle XRD patterns of the catalyst were shown in Fig. 1. The pure siliceous SBA-15 exhibits three well-resolved reflections at 2θ of 0.5–10°, including one strong (1 0 0) peak and two weak peaks (1 1 0) and (2 0 0). Post-synthesize grafting of Fe, Fe–Cr and Cr species into pure siliceous SBA-15 decreases the intensity of the diffraction peaks to some extent. The decrease in intensity becomes noticeable when the Fe, Fe–Cr and Cr content is more than 10 wt.%, although the hexagonal reliability of SBA-15 support is still accomplished. The decrease in peak intensity suggests the irregular organization at long range order of the mesoporous structure, arising from either the incorporation of Fe, Cr and Fe–Cr species into the channels. These results suggest that the procedures for grafting Fe, Cr and Fe–Cr into SBA-15 preserve the long range order of the mesoporous structure probably due to the anhydrous condition and hydrophobicity of SBA-15 pore wall surface [20].
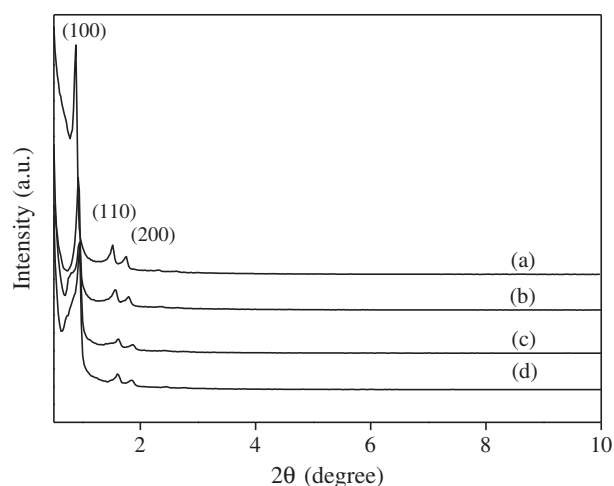

Fig. 1. Low-angle X-ray diffraction patterns of mesoporous molecular sieves: (a) pure siliceous SBA-15, (b) Fe-SBA-15, (c) Cr-SBA-15 and (d) Fe–Cr-SBA-15.

Fig. 2 shows the high angle XRD patterns of the catalysts. It is observed that Fe, Cr and Fe–Cr crystalline phase is absent when the Fe, Fe–Cr and Cr content are 10 wt.% or less. In this method, Fe, Fe–Cr and Cr grafting occurs through silanol groups. Therefore, it is reasonable to suggest that Fe, Fe–Cr and Cr species are incorporated into the SBA-15 channels due to the preferential reaction between Fe, Fe–Cr and Cr precursors and silanol groups on the pore wall surfaces.

3.1.2. N_2 sorption isotherms

N_2 sorption isotherm is the primary technique used to measure the average physical properties of mesoporous molecular sieves. N_2 sorption isotherm of pure siliceous SBA-15, Fe-SBA-15, Fe–Cr-SBA-15 and Cr-SBA-15 are shown in Fig. 3. The isotherm of pure siliceous SBA-15 presented a sharp inflection at relative pressure in the range of 0.6–0.8, an indication of the good quality SBA-15 materials with a uniform mesoporous structure. Upon grafting Fe, Fe–Cr and Cr, the shape of the isotherms of Fe-SBA-15, Fe–Cr-SBA-15 and Cr-SBA-15 was almost identical to the unique pure siliceous SBA-15, having the sharp capillary condensation step in the range of 0.6–0.8. The similar isotherm shapes of Fe-SBA-15, Fe–Cr-SBA-15 and Cr-SBA-15 and the original pure siliceous SBA-15 suggests the uniform mesoporous structure. The capillary condensation step of the isotherm occurred at lower relative pressure for Fe-SBA-15, Fe–Cr-SBA-15 and Cr-SBA-15 as compared to the calcined pure siliceous SBA-15, indicating decrease of mean pore diameter after Fe, Fe–Cr and Cr loading. The decrease of pore diameter after Fe, Fe–Cr and Cr loading is mostly result from the reconstruction due to dehydroxylation rather than the additional layer of Fe, Fe–Cr and Cr formed inside of the silica wall. The physical properties of pure siliceous SBA-15 and Fe-SBA-15, Fe–Cr-SBA-15 and Cr-SBA-15 obtained from N_2 sorption isotherm are given in Table 1. The BET surface area and

Table 1
Structural and textural properties of mesoporous pure siliceous SBA-15, Fe-SBA-15, Fe–Cr-SBA-15 and Cr-SBA-15.

Catalyst	Unit cell parameter a_o (nm)[a]	Surface area (m² g⁻¹)[b]	Pore size (nm)[b]	Pore volume (cc g⁻¹)[b]	Metal content[c] (wt.%)	Metal content[d] (wt.%)
Pure Si-SBA-15	12.7	801	5.23	0.79	—	—
Fe-SBA-15	12.1	765	4.69	0.66	6	5.8
Fe–Cr-SBA-15	11.8	732	4.12	0.64	3:3	5.6
Cr-SBA-15	11.9	748	4.52	0.63	6	5.7

[a] The values obtained from XRD analysis.
[b] The values obtained from N_2 sorption studies.
[c] Metal content used in the siliceous SBA-15 (Metal = Fe, Fe–Cr and Cr).
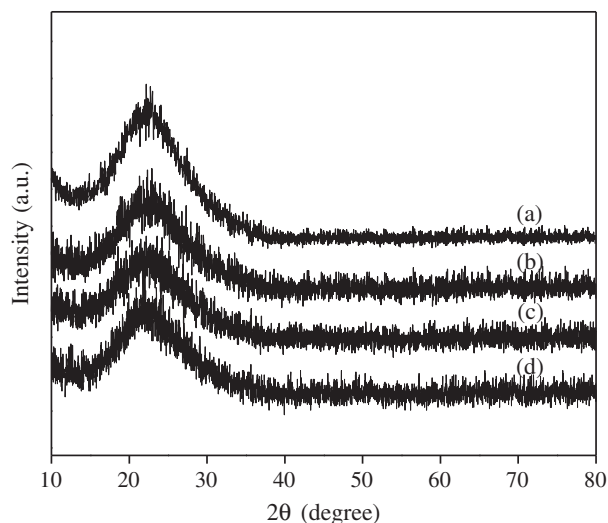[d] Metal content measured by ICP-AES analysis.

Fig. 2. Wide angle X-ray diffraction patterns of mesoporous molecular sieves: (a) pure siliceous SBA-15, (b) Fe-SBA-15, (c) Cr-SBA-15 and (d) Fe−Cr-SBA-15.

Fig. 4. Pore size distribution of mesoporous molecular sieves: (a) pure siliceous SBA-15, (b) Fe-SBA-15, (c) Cr-SBA-15 and (d) Fe−Cr-SBA-15.

pore volume for the pure siliceous SBA-15 are typical for siliceous SBA-15 synthesized under similar conditions. Both the BET surface area and the total pore volume dropped after Fe, Fe−Cr and Cr loading. Fe, Fe−Cr and Cr particles may cause a partial collapse of the mesoporous structure during grafting and recalcination or from the condensation of silanol groups on the surface.

The pore size distribution desorption isotherm branches are shown in Fig. 4. The siliceous SBA-15, Fe-SBA-15, Fe−Cr-SBA-15 and Cr-SBA-15 displayed very sharp pore size distribution. The pore size distribution of Fe-SBA-15, Fe−Cr-SBA-15 and Cr-SBA-15, resembled the mono-model shape in which a smaller mesopore distribution was produced. The mono-model pore distribution of Fe-SBA-15, Fe−Cr-SBA-15 and Cr-SBA-15 are believed to be caused by heterogeneity.

3.1.3. TEM studies

The TEM images of Fe-SBA-15, Fe−Cr-SBA-15 and Cr-SBA-15 samples are shown in Fig. 5. All the TEM images clearly reveal the highly ordered hexagonal arrays of one-dimensional mesopores, typically representing the SBA-15 materials, which is additional
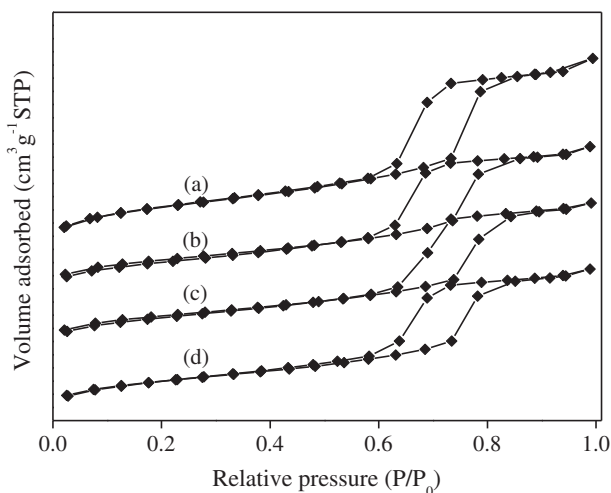

Fig. 3. Nitrogen sorption isotherm of mesoporous molecular sieves: (a) pure siliceous SBA-15, (b) Fe-SBA-15, (c) Cr-SBA-15 and (d) Fe−Cr-SBA-15.
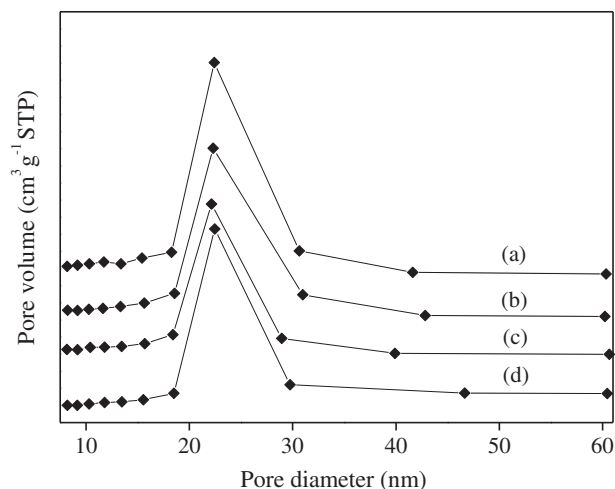
evidence that the ordered SBA-15 framework is retained after grafting and recalcination process. Also, the TEM images do not show the existence of Fe, Fe−Cr and Cr oxide crystals, even on a nanometre scale which indicates that there is no bulk Fe, Fe−Cr and Cr oxide formed on the SBA-15 surface after recalcination. All the Fe, Fe−Cr and Cr ions are believed to be incorporated evenly into the surface of SBA-15 after the grafting and recalcination treatment.

3.2. Growth and characterization of CNTs

3.2.1. Influence of the catalysts

The growth of CNTs carried out using Fe-SBA-15, Fe−Cr-SBA-15 and Cr-SBA-15 molecular sieves at various temperatures such as 700, 800 and 900 °C for 20 min reaction time at the acetylene flow rates of 40 mL min^{-1} were illustrated in Fig. 6. Among the three catalysts, higher carbon deposition yield of 298% was observed with Fe−Cr-SBA-15 and yield might be due to its ability to decompose hydrocarbon like acetylene. Once the reduced atoms reach the pore wall surface they start to nucleate into clusters of increasing size before they initiating the growth of CNTs. During the course of the reaction period very small metal clusters which are not active for CNT growth would likely to be present in the pores. The growth of Fe−Cr clusters likely ceases once their surface is covered with carbon. Therefore, the optimum size and the size distribution of the metal clusters are controlled by the relative rates of several physical and chemical processes which in turn affect the structure and state of the catalysts during the CNTs growth mechanism. It is likely a minimum size is required for the metallic Fe−Cr cluster to initiate the growth of CNTs. Fe−Cr-SBA-15 is chosen to carry out further studies since it produced the maximum carbon deposits while compared to Fe-SBA-15 and Cr-SBA-15.

3.2.2. Influence of the temperature

Fig. 6 shows that the CNTs growth rate over Fe−Cr-SBA-15 at different temperature such as 700, 800 and 900 °C. The carbon deposits yield increases dramatically in the beginning with the temperature up to 800 °C and then decreases with further increase to 900 °C. This decrease might be associated with high vaporization of carbon formed from the decomposition of acetylene as well as agglomeration of catalysts particles at 900 °C. As the temperature increases, the average diameter of CNTs also increases. At lower growth temperature of 700 °C, the CNTs formed are less dense due
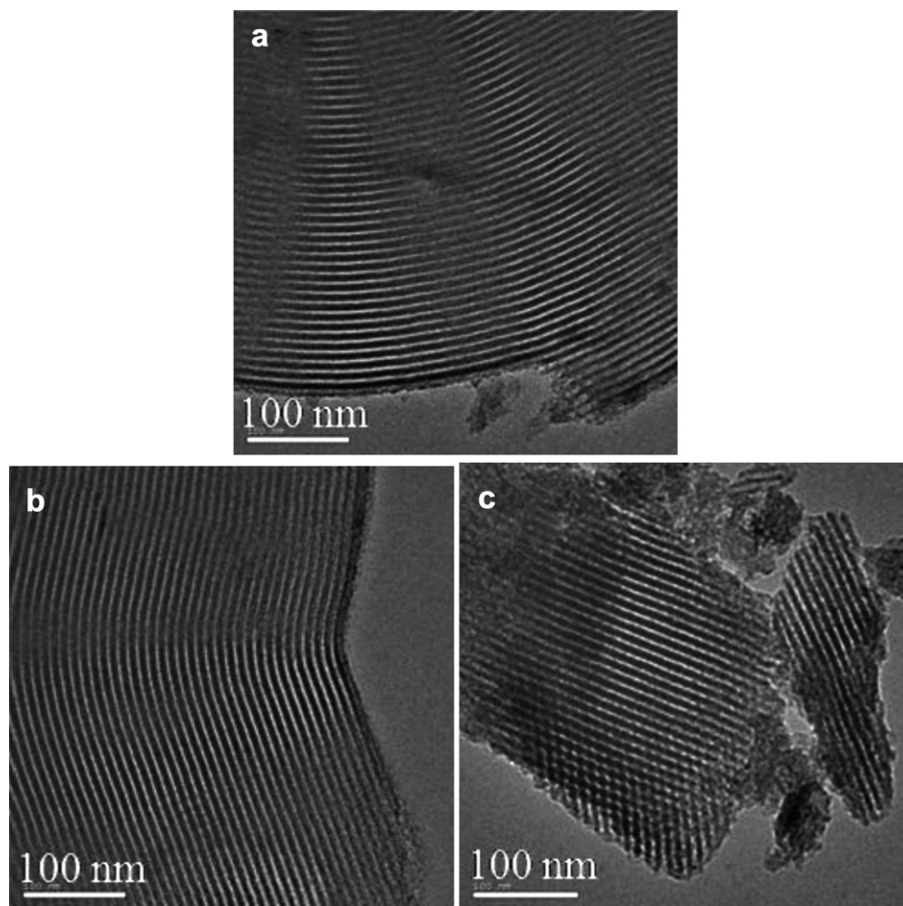
Fig. 5. TEM images of: (a) Fe-SBA-15, (b) Cr-SBA-15 and (c) Fe–Cr-SBA-15.

to slow rate of carbon diffusion in metal as well as slow carbon deposition rate [21]. Another reason for dense CNTs may be due to the non-availability of Fe–Cr particles which might not be reduced at such a low temperature. Moreover, the CNTs grown at 800 °C exhibits uniform diameter and higher density than that of 700 and 900 °C. It is realized that the decomposition rate of acetylene and deposition rate of carbon atoms on the metal particles reach a balance at 800 °C. It is clear that the metal particles are possibly

incorporated homogeneously into the support and leads to production of CNTs in large quantities. Meanwhile, at 900 °C more amorphous carbon and carbonaceous impurities are observed. It is reasonable because larger metal particles are inactive towards the growth of CNTs and only favours the formation of amorphous carbon.

3.2.3. Influence of carbon flow rate

It is well known that flow rate of acetylene plays a vital role in determining the carbon deposition yield and other carbon impurities formation. Hence, the reaction temperature and time maintained at the optimized condition of 800 °C for 20 min while flow rate of acetylene was varied from 10 to 60 mL min^{-1}. The optimized flow rate is found to be 40 mL min^{-1} where the carbon yield attains 298% of CNTs with less amounts of impurities like amorphous carbon. We have expected that the amorphous carbon would not be found when a low flow rate of acetylene (i.e. 10–40 mL min^{-1}) is employed. But we found some amount of amorphous carbon even at this low flow rate of acetylene because some metal particles are not bound to SBA-15 which are responsible for the addition of amorphous carbon. The amount of amorphous carbon is found to be increased when the carbon source supply exceeds 50 mL min^{-1}. This may be probably due to the reduction of metal oxides to a metallic form leading to the formation of larger particles.

3.2.4. TEM studies

The TEM images with different magnification of purified CNTs growth over Fe–Cr-SBA-15 catalyst at 800 °C are shown in Fig. 7. The CNTs have uniform diameter and exhibit hollow core structure.
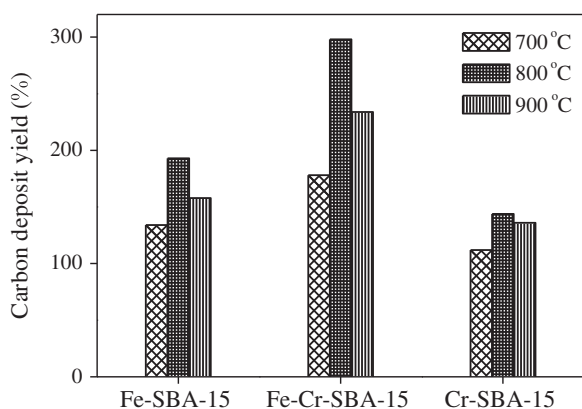

Fig. 6. Effect of reaction temperature on the amount of carbon deposit yield over Fe-SBA-15, Fe–Cr-SBA-15 and Cr-SBA-15 catalyst (catalyst: 100 mg, acetylene: 40 mL min^{-1}, argon: 110 mL min^{-1}, hydrogen: 110 mL min^{-1} and reaction time: 20 min).
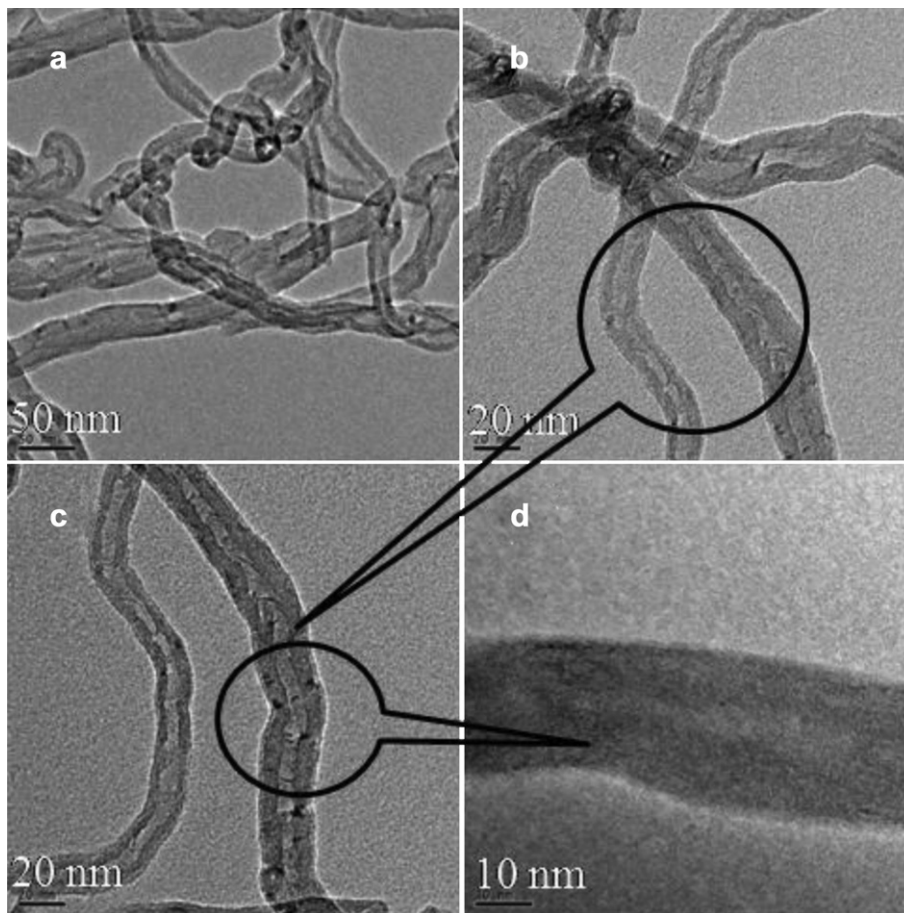
Fig. 7. TEM images of CNTs grown over Fe–Cr-SBA-15 catalyst.

It can be observed from TEM images that high purity CNTs with a diameter of about 8–10 nm and free from amorphous carbon have been obtained using Fe–Cr-SBA-15 catalyst at optimized reaction temperature of 800 °C. The reduced Fe–Cr particles are expected to stay on the surface of the silica spheres homogeneously, which assured continues growth of CNTs during synthesis. The density of the CNTs is high at 800 °C due to the uniform diffusion of carbon atoms on the catalyst particles which are distributed on the SBA-15 support with high density. In addition, there are some catalyst particles observed inside the CNTs or attached at the ends of the CNTs. It is speculated that the catalyst particles might be detached from the silica sphere during the chemical vapour deposition. Further study is needed to confirm the growth mechanism. The result suggests that it is possible to produce clean and well-graphitized CNTs with uniform diameter by this method.
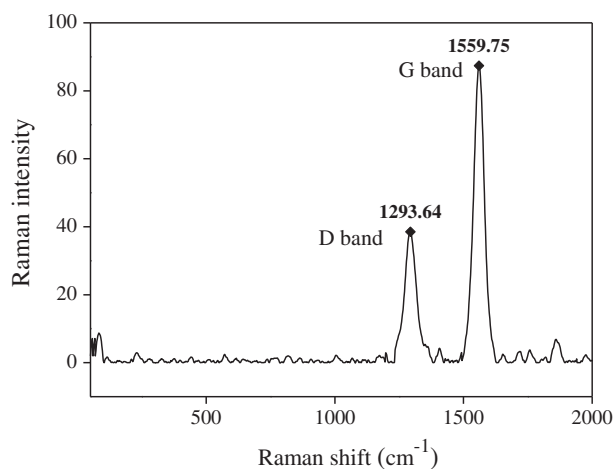

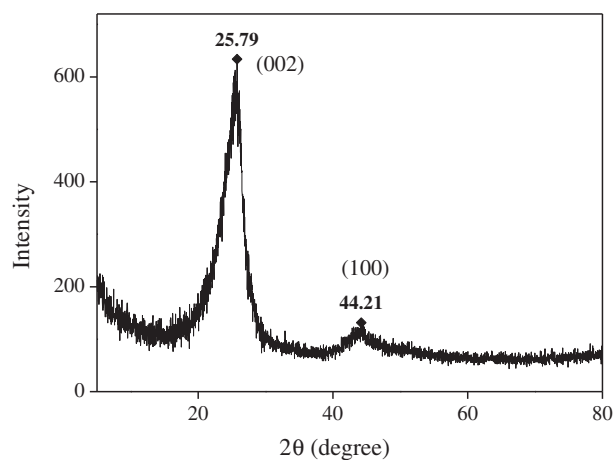**Fig. 8.** Raman spectrum of CNTs grown over Fe–Cr-SBA-15 catalyst.

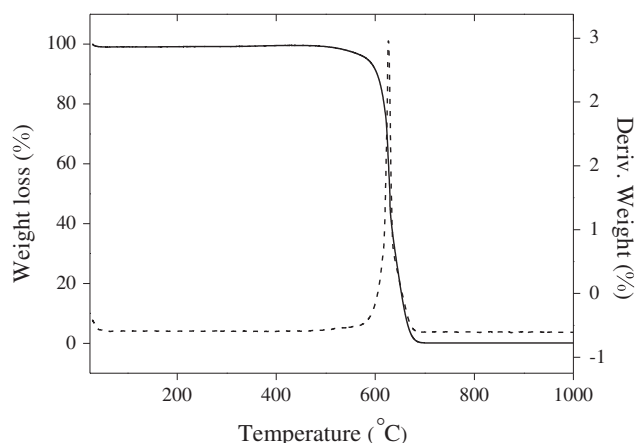**Fig. 9.** XRD patterns of CNTs grown over Fe–Cr-SBA-15 catalyst.

Fig. 10. TGA of purified CNTs grown over Fe–Cr-SBA-15 catalyst.

3.2.5. Raman spectroscopy study

Raman spectrum of the purified CNTs is shown in Fig. 8. In general, the Raman band appearing in the 1500–1605 cm^{-1} region is noted as G band (Graphite band) and the Raman band appearing in the 1250–1450 cm^{-1} region is known as D band (Disorder band). Only two Raman bands appearing in the high wave number region at 1293.6 cm^{-1} and 1559.7 cm^{-1} indicate that the CNTs synthesized in this study are most likely to be multi-walled carbon nanotubes (MWCNTs). The absence of radial breathing modes in the lower wave number region (below 400 cm^{-1}) also confirms the formation of MWCNTs. In addition, the intensity of G band is higher than the D

band and the ratio of I_D/I_G reaches to a minimum for the purified CNTs due to the high purity of the MWCNTs.

3.2.6. X-ray diffraction pattern and thermogravimetric analysis

The high-angle XRD pattern of MWCNTs is shown in Fig. 9. The spectrum displays a strong peak at $2\theta = 25.79°$ and weak peak at $2\theta = 44.21°$, which are assigned to (002) and (100) diffraction patterns of typical graphite respectively.

The thermal stability of purified MWCNT sample is analyzed by TGA in static air shown in Fig. 10. The combustion of MWCNTs takes place between 500 and 620 °C which confirms that the obtained MWCNTs are free from carbonaceous impurities after acid treatment and air oxidation. The result shows that the decomposition temperatures of MWCNTs were higher than that of amorphous carbon and single walled carbon nanotubes (SWCNTs) due to construction of walls. This observation can be ascertained from Fig. 10.

3.2.7. Electrochemical measurement

Cyclic voltammogram analyzes the relationship between ion diffusivity and reaction kinetics of an electrochemical system applied to the different electrodes. Two pairs of redox waves are observed in Fig. 11a. The two anodic and cathodic peaks represent the following Eq. (2) and Eq. (3).

$$3I^- \leftrightarrow I_3^- + 2e^- \tag{2}$$

$$I_3^- + 2e^- \leftrightarrow 3I^- \tag{3}$$

The relative positive pair is assigned to the redox reaction of I_2/I_3^- and the negative one is associated with the reaction of I_3^-/I^-. The redox current density of I_3^-/I_2 at CNTs electrode is much higher than
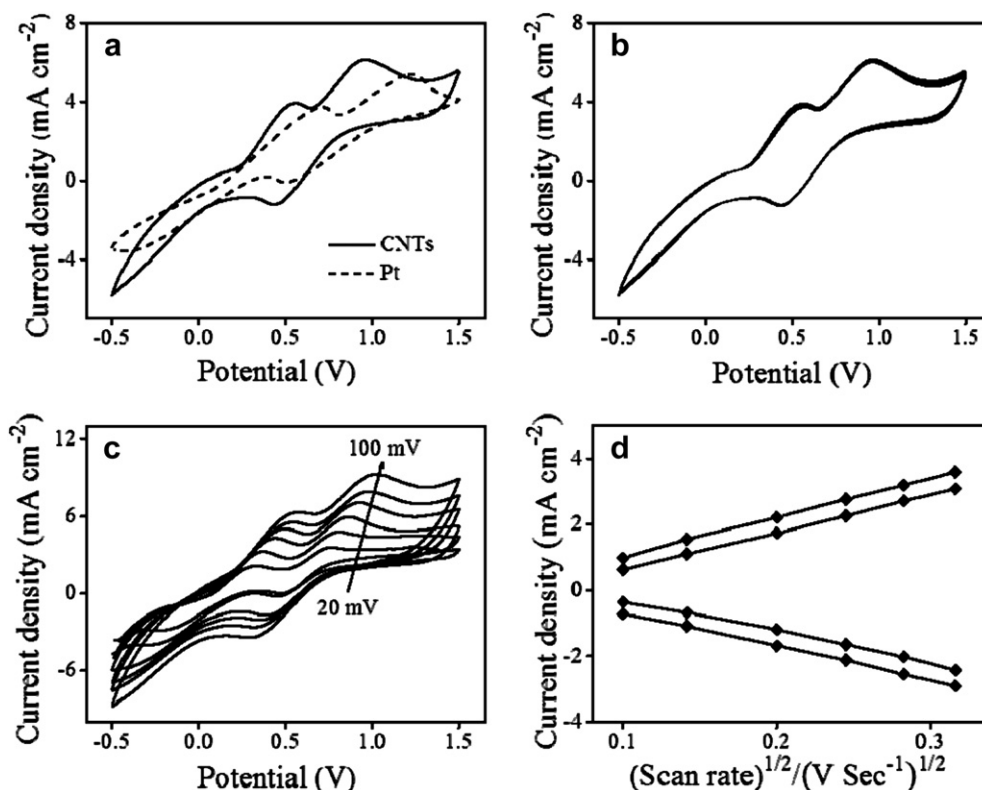

Fig. 11. (a) Cyclic voltammograms for Pt and CNTs electrodes in 0.01 M LiI, 0.001 M I$_2$ and 0.1 M LiClO$_4$ acetonitrile solutions at scan rate of 50 mV s^{-1}, (b) 100 consecutive cyclic voltammograms of CNTs electrode in 0.1 mM LiI, 0.05 M I$_2$ and 0.5 M 4-tertiary butyl pyridine in acetonitrile. Scan rate 50 mV s^{-1}, (c) cyclic voltammograms of the CNTs electrode in 0.01 M LiI, 0.001 M I$_2$ and 0.1 M LiClO$_4$ acetonitrile solutions with different scan rates from inner to outer: 20, 40, 50, 60, 80 and 100 mV s^{-1}. (d) Relationship between the redox peak current and scan rates.
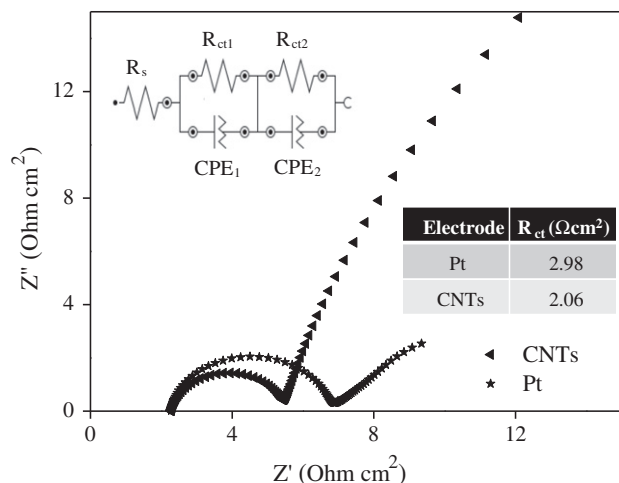
Fig. 12. Impedance spectra of CNTs/Pt symmetric cell.

Electrode	R_{ct} (Ωcm^2)
Pt	2.98
CNTs	2.06

Table 2
Photovoltaic parameters for dye-sensitized solar cells based on different counter electrodes under 100 mW cm^{-2} illumination.

Counter-electrode	J_{sc} (mA cm^{-2})	V_{oc} (V)	FF	η (%)	Ref.
CNT	12.2	0.62	0.51	3.88	[24]
MWCNTs	15.64	0.78	0.62	7.59	[11]
MWCNTs	16.20	0.74	0.64	7.67	[3]
DWCNTs	10.75	0.68	0.53	6.05	[18]
CNTs	14.78	0.74	0.65	7.03	[25]
GMWCNTs	5.6	0.76	0.70	3.0	[9]
CNF	12.1	0.83	0.70	7.0	[26]
GMWCNT	8.95	0.72	0.70	4.46	[27]
Graphene	16.99	0.75	0.54	6.81	[28]
MWCNTs	7.01	0.64	0.54	2.68	[29]
Pt	13.71	0.77	0.82	8.84	This work
MWCNTs	14.24	0.77	0.83	8.86	This work

those in Pt electrode indicating that the former electrode has stronger electrocatalytic activity towards the reduction of I$_3^-$. Fig. 11b shows 100 consecutive cyclic voltammograms in 0.1 mM LiI, 0.05 M I$_2$ and 0.5 M 4-tertiary butyl pyridine in acetonitrile. The cyclic voltammograms do not change and still show stable peak currents indicating that the CNTs fabricated on FTO has excellent electrochemical stability. Fig. 11c shows cyclic voltammograms of the I$_3^-$/I$^-$ system on the CNTs electrode with different scan rates (20–100 mV s^{-1}). With an increase in scan rate the cathodic peak potential shifted towards negative direction and the corresponding anodic peak potential shifted towards positive direction. Eventually the good linear relationship between cathodic and anodic peak current densities (Fig. 11d) versus square root of scan rates indicated the diffusion limitation of the redox reaction on CNTs electrode surface [22,23].

Electrochemical impedance spectroscopy technique has been used to evaluate the catalytic activity of CNTs/Pt counter electrode towards the reduction of I$_3^-$ to I$^-$. The EIS of CNTs/Pt based symmetric cells are compared in Fig. 12. It can be noticed that the charge-transfer resistance (R_{ct}) of Pt electrode is higher than the R_{ct} of CNTs electrode as listed in the inset of Fig. 12. The R_{ct} change in this study essentially refers to the component of resistance against electron transfer from the counter electrode to I$_3^-$. The smallest R_{ct} value of CNTs/FTO associates well with the highest J_{sc} value
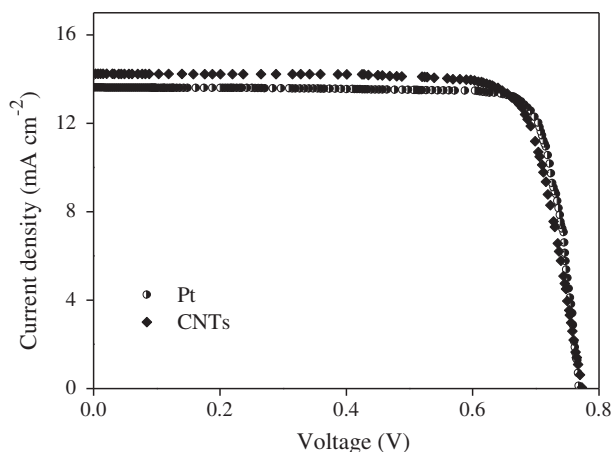
obtained for corresponding DSSCs. EIS result indicates that the CNTs can efficiently catalyze the reduction of I$_3^-$ to I$^-$. The high surface area of CNTs can considerably improve the catalytic activity of the counter electrode. The increased fill factor (FF) of DSSCs with CNTs counter electrode compared with those of cells with Pt counter electrode also supports this examination. It is known that FF depends on the resistances of the photoanode, electrolyte and counter electrode. The higher FF of CNTs electrode was due to high charge-transfer rate and low sheet resistance.

3.2.8. DSSC photovoltaic performance

The j–V curves of DSSCs based on our CNTs and standard Pt counter electrodes are shown in Fig. 13. The open circuit potential (V_{oc}), short circuit current density (J_{sc}), FF, and conversion efficiency (η) of all cells are presented in Table 2. The DSSCs using Pt as counter electrode had J_{sc} of 13.71 mA cm^{-2}, V_{oc} of 0.77 V, FF of 0.82 and η of 8.84% whereas DSSCs using CNTs as counter electrode achieved J_{sc} of 14.24 mA cm^{-2}, V_{oc} of 0.77 V, FF of 0.83 and η of 8.86%. For comparison purpose, the light-to-electric energy efficiencies of the DSSCs with different counter electrodes are summarized in Table 2. As can be seen from Table 2, the performance of DSSC fabricated with counter electrode based on MWCNTs synthesized in the present work displayed superior performance compared to most of the earlier reports. The origin of such a high electrocatalytic activity of MWCNTs electrodes can be originated from the large surface area provided by the MWCNTs [3,30,31]. The superior performance of MWCNTs based counter electrode developed in the present study proved that device grade MWCNTs can be conveniently prepared in bulk by chemical vapour deposition using Fe–Cr-SBA-15 catalyst.

4. Conclusions

High-surface area and well-ordered mesoporous Fe–Cr-SBA-15 catalyst is successfully synthesized by post synthesis grafting in order to prepare well-graphitized CNTs with uniform diameter. Physico-chemical properties of Fe–Cr-SBA-15 are characterized by low and high angle XRD, N$_2$ sorption isotherm and TEM analysis. The surface area, pore size and pore volume of calcined siliceous SBA-15 decreased upon grafting of Fe and Cr from 801 to 732 m^2 g^{-1}, 5.23 to 4.12 nm and 0.79 to 0.64 cc g^{-1}, respectively. The Fe–Cr-SBA-15 shows high reduction stability and high thermal as well as hydrothermal stability. It is found that the CNTs growth rate is maximum at the high temperature of 800 °C. Under the optimized conditions of 800 °C growth temperature, 40 mL min^{-1} acetylene flow rate and 20 min reaction period, the Fe–Cr-SBA-15 yield is 298% carbon deposit. TEM analysis reveals that the CNTs with a diameter of 8–10 nm are obtained. The ratio of I_D/I_G reaches to a minimum value that confirms the formation of high quality

Fig. 13. Photocurrent voltage (j–V) characteristics of DSSCs fabricated with CNTs- and Pt-based counter electrode.

MWCNTs. The TGA result also confirms the formation of high quality, amorphous free MWCNTs. Finally, CNTs synthesized in the present investigation is applied as a counter electrode in DSSCs. CNTs based counter electrode shows better performance than Pt based counter electrode.

Acknowledgements

References

[1] M. Gratzel, Nature 414 (2001) 338–344.
[2] P. Sudhagar, J.H. Jung, S. Park, R. Sathyamoorthy, H. Ahn, Y.S. Kang, Electrochim. Acta 55 (2009) 113–117.
[3] W.J. Lee, E. Ramasamy, D.Y. Lee, J.S. Song, ACS Appl. Mater. Interfaces 1 (2009) 1145–1149.
[4] G. Veerappan, K. Bojan, S.W. Rhee, ACS Appl. Mater. Interfaces 3 (2011) 857–862.
[5] F. Sauvage, D.H. Chen, P. Comte, F.Z. Huang, L.P. Heiniger, Y.B. Cheng, R.A. Caruso, M. Gratzel, ACS Nano 4 (2010) 4420–4425.
[6] W.J. Lee, E. Ramasamy, D.Y. Lee, J.S. Song, Sol. Energy Mater. Solar Cells 92 (2008) 814–818.
[7] H.Y. Wang, F.M. Wang, Y.Y. Wang, C.C. Wan, B.J. Hwang, R. Santhanam, J. Rick, J. Phys. Chem. C 115 (2011) 8439–8445.
[8] C.S. Chou, C.I. Huang, R.Y. Yang, C.P. Wang, Adv. Powder Technol. 21 (2010) 542–550.
[9] H. Choi, H. Kim, S. Hwang, W. Choi, M. Jeon, Sol. Energy Mater. Solar Cells 95 (2011) 323–325.
[10] S.H. Seo, S.Y. Kim, B.K. Koo, S.I. Cha, D.Y. Lee, Langmuir 26 (2010) 10341–10346.
[11] E. Ramasamy, W.J. Lee, D.Y. Lee, J.S. Song, Electrochem. Commun. 10 (2008) 1087–1089.
[12] D. Zhao, J. Feng, Q. Huo, N. Molish, G.H. Fredrickson, B.F. Chmelka, G.D. Stucky, Science 279 (1998) 548–552.
[13] R. Ryoo, C.H. Ko, M. Kruk, V. Antochshuk, M. Jaroniec, J. Phys. Chem. B 104 (2000) 11465–11471.
[14] K. Hernadi, A. Fonseca, J.B. Nagy, A. Siska, I. Kiricsi, Appl. Catal. A Gen. 199 (2000) 245–255.
[15] J. Kong, A.M. Cassele, H. Dai, Chem. Phys. Lett. 292 (1998) 567–574.
[16] C.N.R. Rao, B.C. Satishkumar, A. Govindaraj, M. Nath, ChemPhysChem. 2 (2001) 78–105.
[17] J. Duxiao, H. Nongyue, Z. Yuanying, X. Chunxiang, Y. Chunwei, L. Zuhong, Mater. Chem. Phys. 69 (2001) 246–251.
[18] D.W. Zhang, X.D. Li, S. Chen, F. Tao, Z. Sun, X.J. Yin, S.M. Huang, J. Solid State Electrochem. 14 (2010) 1541–1546.
[19] H.C. Sun, Y.H. Luo, Y.D. Zhang, D.M. Li, Z.X. Yu, K.X. Li, Q.B. Meng, J. Phys. Chem. C 114 (2010) 11673–11679.
[20] C. Wang, S.Y. Lim, G.A. Du, C.Z. Loebicki, N. Li, S. Derrouiche, G.L. Haller, J. Phys. Chem. C 113 (2009) 14863–14871.
[21] A.N. Usoltseva, V.L. Kuznetsov, A.L. Chuvilin, N.A. Rudina, M.Y. Alekseev, L.V. Lutsev, Carbon 42 (2004) 1037–1042.
[22] S. Biallozor, A. Kupniewska, Electrochem. Commun. 2 (2000) 480–486.
[23] A. Hauch, A. Georg, Electrochim. Acta 46 (2001) 3457–3466.
[24] H.J. Shin, S.S. Jeon, S.S. Im, Synth. Met. 161 (2001) 1284–1288.
[25] G. Zhu, L. Pan, T. Lu, X. Liu, T. Lu, T. Xu, Z. Sun, Electrochim. Acta 56 (2011) 10288–10291.
[26] G. Veerappan, W. Kwon, S.W. Rhee, J. Power Sources 196 (2011) 10798–10805.
[27] H. Choi, H. Kim, S. Hwang, M. Kang, D.W. Jung, M. Jeon, Scr. Mater. 64 (2011) 601–604.
[28] D.W. Zhang, X.D. Li, H.B. Li, S. Chen, Z. Sun, X.J. Yin, S.M. Huang, Carbon 49 (2011) 5382–5388.
[29] J. Luo, H.J. Niu, W.J. Wu, C. Wang, X.D. Bai, W. Wang, Solid State Sci. 14 (2012) 145–149.
[30] J.M. Nugent, K.S.V. Santhanam, A. Rubio, P.M. Ajayan, Nano Lett. 1 (2001) 87–91.
[31] C.E. Banks, T.J. Davies, G.G. Wildgoose, R.G. Compton, Chem. Commun. 7 (2005) 829–841.

Nomenclature

a_o: unit cell parameter
a.u.: arbitrary unit
CPE: constant phase element
j: current density (A cm^{-2})
J_{sc}: short circuit current density (mA cm^{-2})
S_{BET}: BET Surface area (m^2 g^{-1})
P: pressure (Pa)
P/P_0: relative pressure
R_s: solution resistance (Ω cm^2)
R_{ct}: charge-transfer resistance (Ω cm^2)
STP: standard temperature pressure
V_{oc}: open circuit potential (volt)
Ω: electrical resistance (ohm)
η: conversion efficiency (%)
θ: theta

Abbreviation
SBA-15: santa barbara amorphous no. 15
MCM-41: mobil composition of matter no. 41
CNTs: carbon nanotubes
SWCNTs: single walled carbon nanotubes
DWCNTs: double walled carbon nanotubes
MWCNTs: multi walled carbon nanotubes
GMWCNTs: graphene-multi walled carbon nanotubes
CNF: carbon nanofiber
TBP: 4-tert-butyl-pyridine
P123: poly(ethylene glycol)-block-poly(propylene glycol)-block-poly(ethylene glycol)
TEOS: tetraethoxysilane
ALD: atomic layer deposition
ICP-AES: inductive coupled plasma-atomic emission spectroscopy
BJH method: Barret–Joyner–Halenda method
FF: fill factor
DSSCs: dye-sensitized solar cells